Iranian Journal of Materials Science and Engineering, Vol. 19, Number 4, December 2022

RESEARCH PAPER

Microstructural Behavior and Corrosion Analysis of Lean Duplex Stainless Steel 2101 under the Influence of Variable Heat Inputs Using Gas Tungsten Arc Welding

Sravanthi Gudikandula[1], Ambuj Sharma[2,*]

* *sharma.ambuj@vitap.ac.in*

[1] Research Scholar, School of Mechanical Engineering, VIT-AP University, AP, India
[2] Associate Professor, School of Mechanical Engineering, VIT-AP University, AP, India

Received: May 2022   Revised: October 2022   Accepted: November 2022
DOI: 10.22068/ijmse.2792

Abstract: *The lean duplex stainless steels (LDSS) have excellent features due to the microstructural phase combination of austenite and ferrite grains. These steels have low Ni and Mo contents which can reduce the cost and stabilize the austenite fraction in the microstructure. In recent years, welding is used to enhance the microstructural behaviour of LDSS. In this paper, Gas tungsten arc welding (GTAW) was performed on LDSS S32101 with different heat energy inputs and varying welding currents. The influence of heat inputs (0.85 and 1.3 kJ/mm) on welded samples was investigated to study the microstructural behaviour, phase balance, and mechanical & corrosion performance. The microstructures studies were carried out using an optical microscope, scanning electron microscope and X-ray diffraction. The effect of Heat input led to the significant microstructural evolution in weld metals with high austenite reformation. The microstructure of weldments consisted of inter-granular austenite (IGA), grain boundary austenite (GBA) and Widmanstatten austenite (WA). Important mechanical properties such as tensile strength and micro-hardness were investigated to understand the performance of weldments. The polarization method was used to understand the corrosion behaviour of weldment in a 3.5% NaCl solution. The experimental results showed enhanced properties of welds that could be suitable for industrial applications.*

Keywords: *Lean duplex stainless steel, LDSS 2101, Microstructure, Corrosion resistance, Mechanical properties.*

1. INTRODUCTION

Duplex stainless steels (DSS) have superior mechanical properties and corrosion resistance as compared to conventional austenitic stainless steels, mainly because of their two-phase microstructure which is a combination of austenite and ferrite [1]. However, conventional DSSs contain high amounts of nickel (~ 6%) and molybdenum (~ 3%) which have a high cost and limit their use in commercial applications [2]. So, Lean duplex stainless steel (LDSS) with very low alloying elements (nickel and molybdenum) stands to be a better alternative due to its low cost as compared to conventional DSSs and austenitic stainless steels AISI 304 or AISI 316L [3-4]. These LDSSs are popularly used in the oil & gas industry, desalination plants, paper and pulp industry, pressure vessels, nuclear and marine industries where mechanical and corrosion properties are of primary importance [5].

The main alloying elements of LDSS2101 are 21.5Cr, 5Mn, 1.5Ni, 0.22N and 0.3Mo which have good mechanical strength and corrosion resistance [6]. This newly developed lean duplex grade is cost effective because of low Ni content which stabilized the austenite fraction in the microstructure. The low content of Ni is balanced by the addition of 0.22% Nitrogen and 5% Manganese in LDSS2101 to maintain a good microstructure with a phase ratio of ferrite and austenite. Also, Mo element is decreased in this grade to limit the deleterious phase precipitation [7]. The material strength of this grade is similar to duplex steel grade DSS 2205 (EN 1.4462). Corrosion performance of LDSS2101 is higher than AISI 304 steel and pitting resistance is better than AISI 316 steel [4], [7], [8], [9].

Gas tungsten arc welding (GTAW) is mostly used as a joining process in fabrication industries. GTAW ensures the functional requirements of the weld joint as closest to the base material and has better mechanical properties [10]. In general, filler wires are utilized for welding the stainless steel and they are over-alloyed with Ni to promote the austenite formation in weld zone [11]. All types of fusion welding methods are used in LDSS. However, care must be taken to maintain the required balance between the two phases (austenite and ferrite) in the weld zone, otherwise

[DOI: 10.22068/ijmse.2792]

the mechanical and corrosion properties of the weld metal will be adversely affected compared to the base metal. The phase balance in the weld zone depends on the welding parameters and heat input employed during DSS welding [12-14].

The other important factor to be considered during welding is to avoid secondary phase precipitation which degrade the mechanical properties and corrosion performance [15-16]. Amigó et al have investigated microstructural and mechanical properties with variation in laser welding parameters of Thyssen NIROSTA 4462 DSS [17]. They reported a drastic decrease in the mechanical properties of the laser weld with increasing welding speed, which was correlated to changes in the ferrite to austenite ratio due to weld cooling rate variations. Faster cooling rates result in higher amount of ferrite and slower cooling rates promotes more austenite formation in weld zone. Also, they observed lower heat input may increase ferrite percentage in weld zone, due to the precipitation of chromium nitride phases (CrN and Cr_2N).

A particular ratio of ferrite versus austenite is recommended for improved performance of duplex stainless steel, which is strongly influenced by the welding heat input range [18-19]. Therefore, choice of a suitable welding process that controls the welding heat input and the resulting cooling rates, are always important. The corrosion performance of DSS welds is dependent on the ferrite/austenite phase fraction which can be controlled using welding parameters, shielding gases and pre-weld cleaning conditions [20]. From the literature, many researchers attempted to optimize the welding process parameters to enhance the weld microstructures, mechanical and corrosion performance [21-24]. However, it is challenging to arrive at optimal welding conditions for a relatively newer lean duplex stainless steel LDSS2101, for which a very limited research articles are published. Therefore, in the present work, an attempt has been made to analyze the effect of welding parameters on the microstructure, mechanical properties and corrosion resistance of lean duplex stainless steel (LDSS 2101) weld joints produced by GTAW. Mechanical, corrosion and microstructure analysis revealed promising observations under the different heat inputs.

2. EXPERIMENTAL PROCEDURES

2.1. Experimental Setup

The schematic sketch of the weldment with dimensions is shown in Fig. 1. LDSS 2101 sheet with 8 mm thickness is considered as the base material (BM). GTAW is employed with electrode ER 2209 to produce the weld joints in two passes. A single V-groove with included angle 600 is prepared with machining, and the joint edges are mechanically cleaned with stainless steel rotary brushes [24]. The alloying compositions of BM and electrode are shown in Table 1. Welding parameters considered for the study are shown in Table 2. The heat input is the ratio of total input power to welding speed and is expressed in joules per meter. The following equation is used for the calculation of heat input [25].

$$H=\frac{\eta VI}{v} \quad (1)$$

where η= Efficiency; V= Voltage (volt)s; I= current (Amp) and v= Velocity of heat source (mm/s).

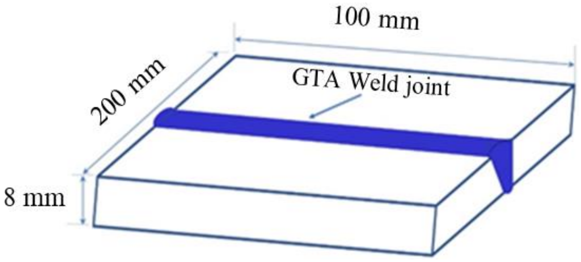

Fig. 1. Schematic sketch of weldment with dimensions.

The primary acceptance criterion for the weldment is consistent and uniform weld penetration without any melt-related defects such as cracks, gas porosity, undercut and lack of sidewall fusion, etc. In the present work two heat inputs namely low heat 0.85 kJ/mm and high heat 1.3 kJ/mm are considered to produce healthy weldments. Welding currents 74A and 86A correspond to 0.85 kJ/mm and 1.3 kJ/mm of heat input. Low heat and high heat welded samples are designated as LH74 and LH86 and shown in Fig. 2. The energy during welding should not be too high to prevent grain growth and maintain the mechanical and corrosion performance of the weld. The flow chart of fabrication strategies and characterization techniques used in this paper is shown in Fig. 3.

[DOI: 10.22068/ijmse.2792]

Table 1. Chemical composition of base LDSS 2101 and ER 2209

Sample	C	Cr	N	Mn	Cu	Si	Ni	Mo	P
LDSS 2101	0.031	21.24	0.24	4.78	0.32	0.68	1.52	0.35	0.03
ER 2209	0.03	21.8	0.13	1.0	0.01	0.9	6.8	3.1	0.026

Table 2. Gas tungsten arc welding process parameters

Sample	Current (A)	Voltage (V)	Heat input (kJ/mm)	Electrode diameter (mm)	Root gap (mm)	Plate distance (mm)	Time for weld (Sec)
Low heat input	74	21	0.85	3.15	2	100	55
High heat input	86	25.2	1.3	3.15	2	100	60

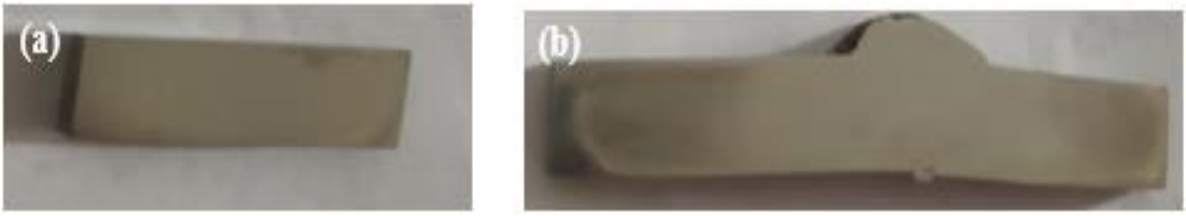

Fig. 2. Images of samples used in present study: base metal (BM) and welded sample

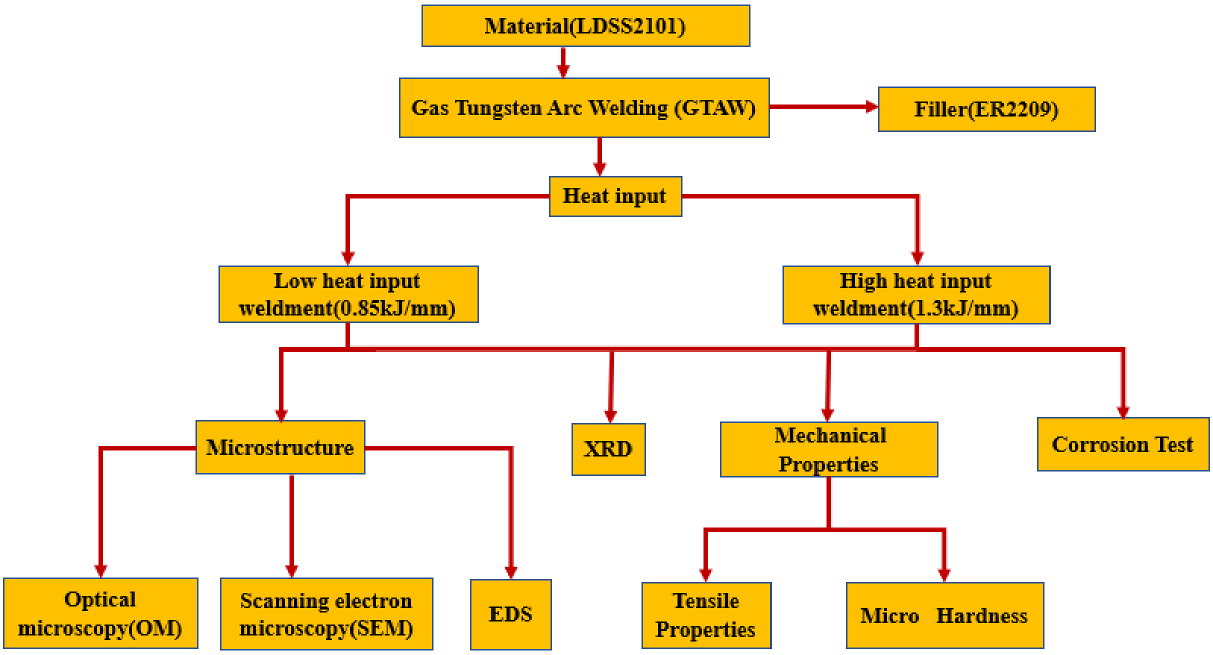

Fig. 3. Flow chart of welding methodology and characterization tools used in the present study.

2.2. Sample Characterization

2.2.1. Microstructural Analysis

The samples for microstructural examination are prepared through a standard metallography method -ASTM E3-95 [26]. Samples are polished with the emery papers (180, 400, 600, 800, 1200, 1500 grit silicon carbide) followed by alumina suspension. Lastly, diamond polishing is done to get a clean and shiny surface. Polished samples are etched with kallings reagent for 20-30 s to get metallographic images under optical microscopy [27]. The different zones of weld joints are examined under OLYMPUS makes an optical metallurgical microscope, and TESCAN makes a scanning electron microelectronic microscope (SEM) with Energy Dispersive x-ray spectrometry (EDS) for localized chemical composition. X-ray diffraction (XRD) analysis is performed to identify the phases of the aged samples using Bruker D2 Phase 2nd generation

[DOI: 10.22068/ijmse.2792]

with Cu (Ka) radiation (0.1540 nm) operating at 40 kV and 40 mA. The obtained patterns are characterized by Xpert High Score software using the PDF4 database.

2.2.2. Corrosion Analysis

The corrosion behaviour of base and welded samples is evaluated through potentiodynamic polarization test, by employing conventional 3-electrode cell. The electrochemical test setup has a saturated calomel electrode (SCE) which acts as a reference electrode, samples for testing act as working electrode and counter electrode is platinum wire. It is carried out at a scan rate of 10 mV/s. Prior to the electro chemical test, the samples are immersed in 3.5% NaCl solution at room temperature for 30 minutes until a steady state open circuit voltage (Ecorr) is attained. The surface area of sample exposed to solution is 0.1257 cm^2.

2.2.3. Mechanical Properties

The tensile test is carried out on SHIMADZU Model- 343-07979-12, capacity of 250 kN. The ASTM standard E8M-04 is followed to perform the tensile test at normal strain rate 2 mm/min at room temperature. The elongation and ultimate strength of the samples have been recorded to estimate the mechanical strength of the weldments. Fractography analysis is also performed on fractured surface of tensile samples to understand the mode of fracture. A microhardness test is carried out to understand the hardness variation in samples. The hardness test is carried out on the Vickers Hardness Tester (METCO VH-1MDX) according to ASTM E9231. A 10 kg load is released for 10-15 sec on the sample surface to measure microhardness.

3. RESULTS AND DISCUSSION

This section illustrates the microstructural characterization results obtained from the optical microscopy, SEM based EDS analysis and XRD analysis. Corrosion behaviour and mechanical properties are also discussed in detail to examine the performance of welded samples.

3.1. Microstructural Analysis

The optical and SEM microstructures of LDX 2101 base metal are shown in Fig. 4(a-b). It is a two-phase microstructure with alternative austenite and ferrite phases. The austenite phase is seen as discontinuous light etched banded regions, and the ferrite phase is the continuous darker matrix. The austenite ferrite phase fraction measured in LDSS base metal shows an approximately 50:50 ratio. The macrostructure of the weldments obtained from 0.85 kJ/mm (LH74) and 1.3 kJ/mm (LH86) heat input conditions are shown in Fig. 5. In the present study, it is observed as ferrite solidification mode and the austenite nucleates below the ferrite conditions [12].

Fig. 6(a-b) represents the weld zone optical images of both LH74 and LH86 samples, and the typical HAZ microstructures are shown in Fig. 7(a-b). The microstructure of both weldments shows that the increase in heat input from low to high range promotes a gradual increase in the amount of austenite phase precipitation. During welding, high heat input (1.3 kJ/mm) undergo a slow cooling rate, resulting in large grain size and higher contents of austenite, whereas the low heat input (0.8 kJ/mm) under a high cooling rate resulted in lower austenite content with more refined grains.

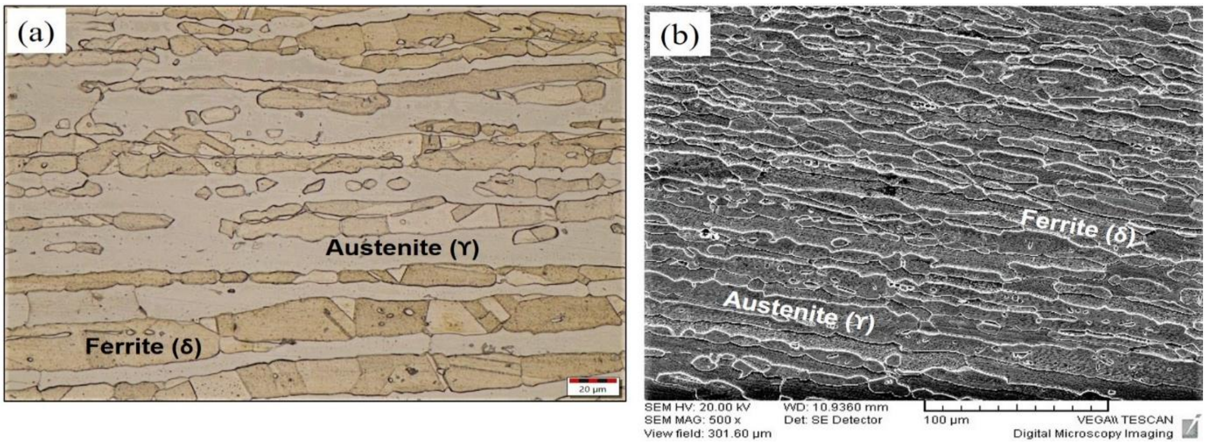

Fig. 4. Microstructures of LDSS 2101 base metal (a) Optical (b) SEM.

[DOI: 10.22068/ijmse.2792]

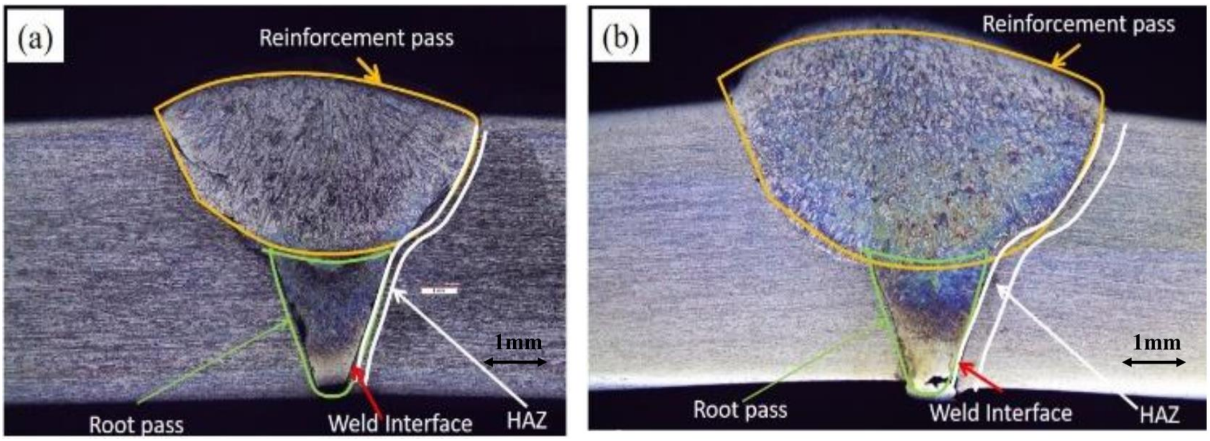

Fig. 5. Optical Macrostructures of weld samples (a) LH74 (b) LH86.

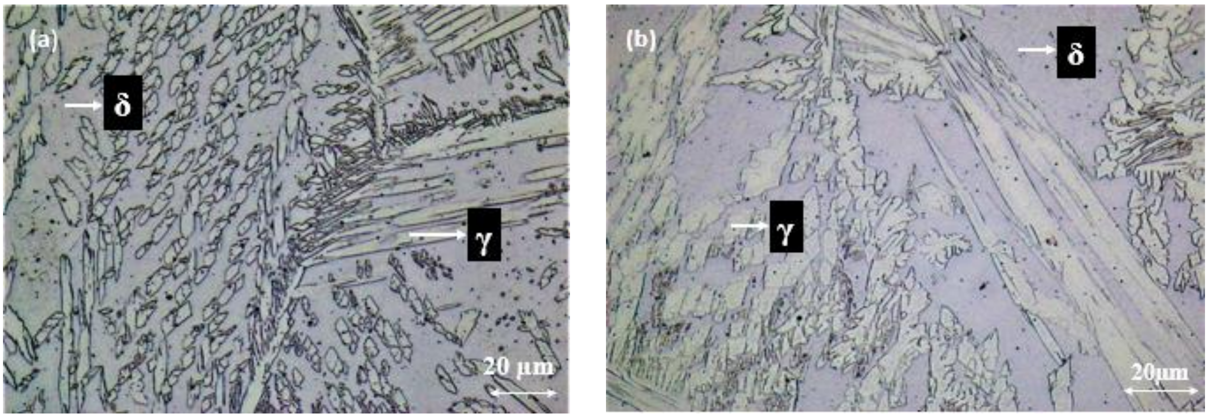

Fig. 6. Optical images of WM: (a) LH74 (b) LH86.

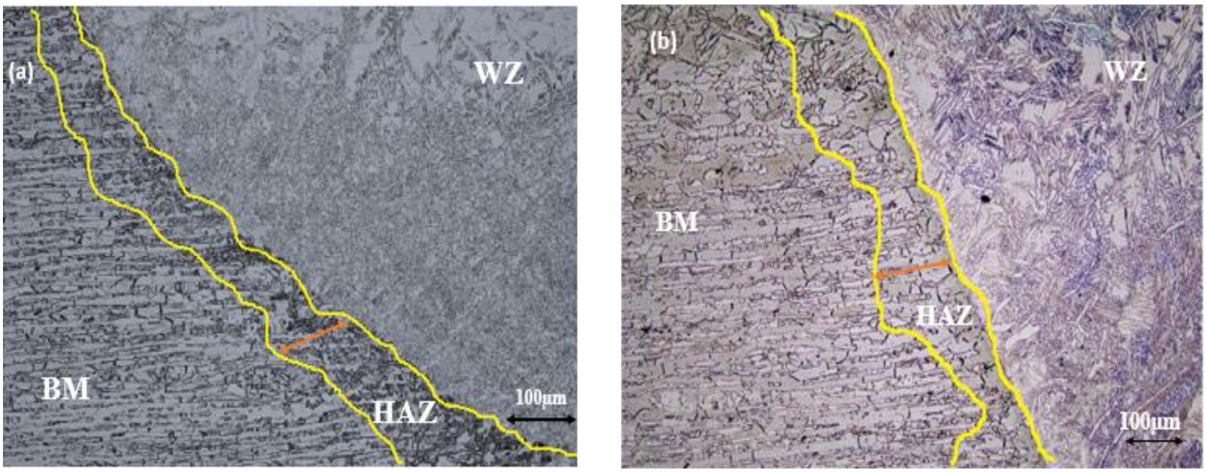

Fig. 7. Optical images of the interface of HAZ/BM of (a) LH74 and (b) LH 86 samples.

The average percentage of the austenite phase volume of the base and welded samples is taken from the image analysis and shown in Fig. 8. The high heat (LH86) and low heat (LH74) input samples show 52.69% and 44.13% austenite phase, respectively. At high heat input, lesser ferrite is formed because of slow cooling rates and indirectly facilitates high austenite formation.

The microstructure of both weld LH74 and LH86 shows similar morphological features such as grain boundary austenite (GBA), inter-granular austenite (IGA), and Widmanstatten austenite (WA) [12-13],[25] [28] and this can be seen in Fig. 9. During weld cooling, initially the grain

[DOI: 10.22068/ijmse.2792]

boundary austenite (GBA) phase is nucleated at the ferrite grain boundaries followed by Widmanstatten secondary austenite and it develops into a ferrite grain with certain angles. Finally, the IGA formed inside the ferrite grains and grew into blocks. The under-cooling degree forms the final microstructure [25] [29]. This study shows that HAZ has coarse ferrite and austenite grains, and there are no intermetallic precipitates.

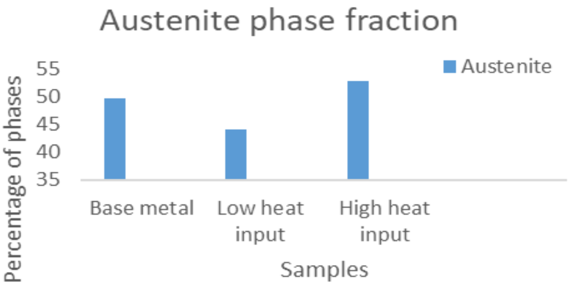

Fig. 8. Samples showing austenite phase fraction.

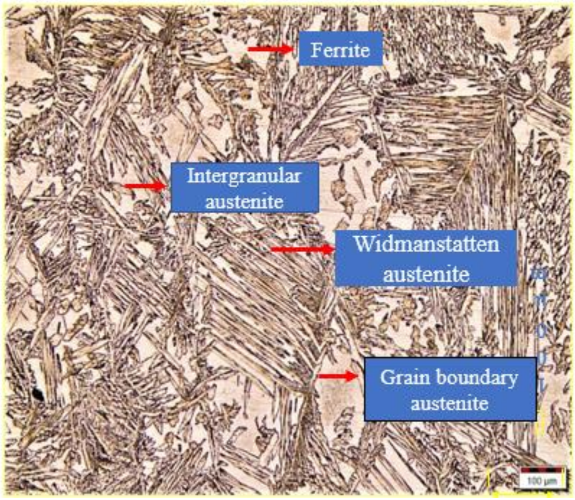

Fig. 9. Optical microstructure of WZ with morphological characteristics: intergranular austenite, grain boundary austenite and Widmanstatten austenite.

Fig. 10(a-b) shows the SEM images corresponding to LH74 and LH86. It is observed that as the heat input increased, the microstructure exhibited a change in grain morphology as compared to the base metal. It can also be seen that insufficient GBA phase formation resulted in the formation of new coarse ferrite-grains. The morphological characteristics of the weldments have changed compared to the base material due to changes in the alloy composition at the weld joint [30-31]. The width of the HAZ is influenced by heat input during welding. It is seen from Fig. 10(a)-(b) that the HAZ width for low heat and high heat input welds are 200 µm and 300 µm respectively. The weld cooling rate is influenced the HAZ width. Grain growth is also dependent on the heat inputs during welding.

SEM-EDS measurements are performed to estimate the alloying elements composition in different regions of both weldments. The principal alloying elements present in the weld zone (WZ) and HAZ are shown in Table 3. From Table 3, it can be seen that the chromium (Cr) element has a slight variation from WZ to HAZ compared to other elements such as Ni and Mn. Higher Mo and Ni content is observed in WZ due to filler material ER2209. Due to the excess formation of austenite phase, Ni element is very high in WZ. The formation of the austenite phase is enhanced by increasing the heat input. This can be explained by the cooling time i.e., low heat input gives high cooling rate with short transformation and high heat input gives slow cooling rate which allows more austenite-ferrite transformation. Hence the diffusion of austenite stabilizing elements such as Ni has increased and more amount of austenite is transferred [25] [32]. Therefore, higher Ni elements are observed in LH86 than in LH74.

3.2. XRD Analysis

Fig. 11 shows the comparison of sample's diffraction patterns for both welds LH74, LH86 and BM samples. The X-ray diffraction patterns depict the presence of ferrite and austenite. The corresponding γ and δ phases are identified with intense peaks.

Table 3. WM and HAZ chemical composition two heat inputs (wt%)

Sample	zone	Cr	Ni	Mo	Mn
base metal		21.35	2.26	-	6.03
LH74	**WM**	23.93	7.46	2.06	2.20
	HAZ	22.04	1.67	-	4.97
LH86	**WM**	23.71	8.29	3.36	2.26
	HAZ	22.57	2.27	-	4.84

[DOI: 10.22068/ijmse.2792]

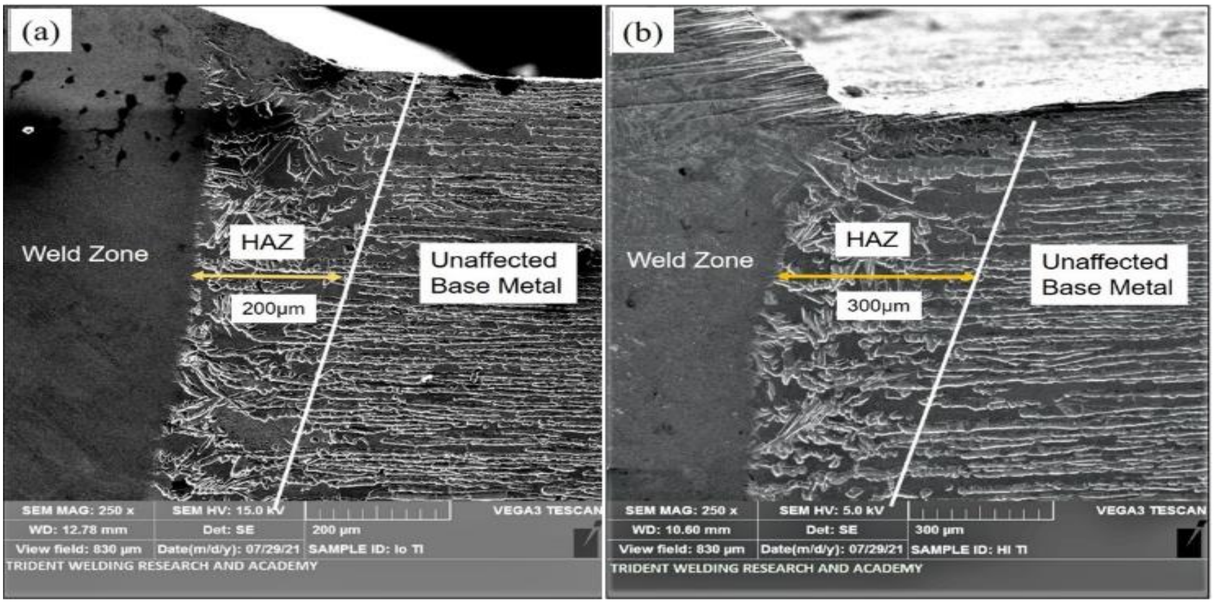

Fig. 10. SEM microstructure of HAZ: (a) LH74 and b) LH86.

There are no precipitates or detrimental phases detected on the XRD spectrum of the weld metals. The low heat input sample LH74 shows optimally balanced ferrite and austenite phases with stronger (111) plane orientation.

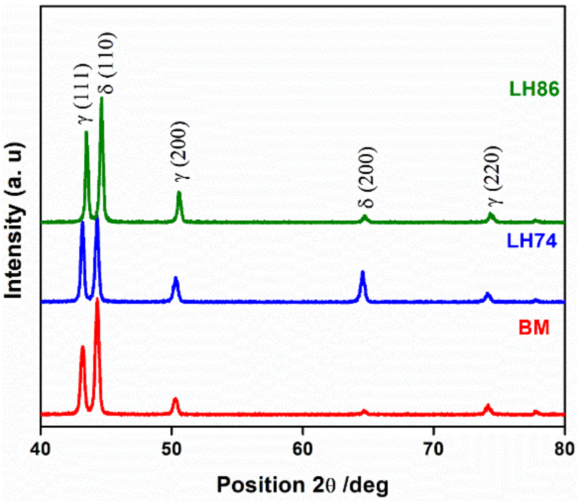

Fig. 11. X-ray diffraction patterns of LDSS 2101 subjected to GTAW heat effected by applied current.

3.3. Hardness Variation

The effect of heat input variation on hardness value is analyzed on LH 74 and LH 86 welded samples and shown in Fig. 12. It is also observed that WZ hardness decreased with increased heat input. This decrease in hardness from low to high heat input in the WZ is due to the cooling rate difference and the phase fraction. As heat input increases, the cooling rate decreases and promotes the γ -austenite formation, leading to a decrease in hardness performance [33]. The hardness value of LH74 and LH86 in WZ are higher than the BM as shown in Fig. 13. It is observed that the weld region exhibited higher hardness than HAZ due to the filler wire and grain refinement. The microhardness values from Fig. 12 show that the LH74 weldment has higher hardness than the LH86 weldment. A high hardness value is noted in the low heat sample (LH74) due to the high cooling rate that leads to grain refinement. In addition, the second reason for the increase in LH74 hardness is the reduced austenite grain size in the weld compared to BM, which is visible in the optical microstructure (in Fig 7) [25].

3.4. Tensile Test

Tensile testing is conducted to evaluate the strength of both LH74 and LH86 weldments. The strength of weld specimens is compared with the BM. Tensile test results are presented in Table 4. From the table, it can be observed that weldments exhibited good strength. The ultimate tensile strength (UTS) of LH74 and LH86 weldments are 705 MPa and 691MPa while BM shows 680 MPa. The weld strength is about 1.6- 3.7% higher than that of the base metal. The low heat input sample LH74 has higher tensile strength than the high heat input sample LH86 due to high cooling rate with refined grains [34]. The yield strength of BM, LH74, and LH86 samples is computed as 495, 528, and 504, respectively.

[DOI: 10.22068/ijmse.2792]

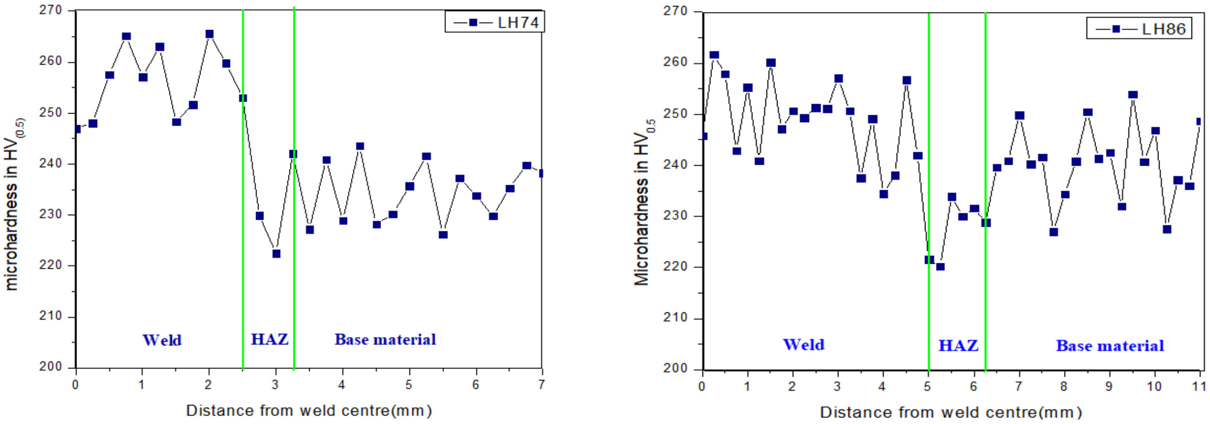

Fig. 12. Hardness profiles of heat input samples

Table 4. Tensile properties of 2101 DSS at GTAW

Specimen	UTS (MPa)	Yield strength (MPa)	% Elongation	Fracture location Centre	Fracture Mode
Base	680	495	28.07%	Centre of gauge length	Ductile
LH 74	705	528	25.3%	HAZ Weld	Ductile
LH 86	691	504	26.8%	HAZ Weld	Ductile

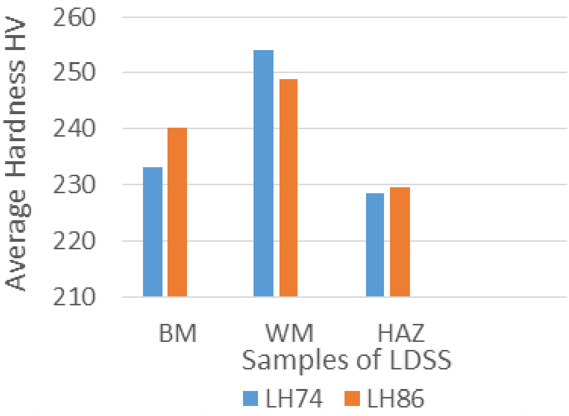

Fig. 13. Average hardness of LDSS 2101 samples.

The yield strength of both weldments is higher due to Ni-based filler ER2209, which probably promotes the strength in the weldment. Percentage elongation of LH74 and LH86 weldments is observed ~5-10% lower than the base metal. The fractography analysis is done to understand the failure behavior of both weldments. The necking phenomenon indicated that the samples exhibited plastic deformation before fracture. The weldments fractured from HAZ to the weld region. The fractography image of a failed LH74 sample under tensile test is shown in Fig. 14. The fractography analysis revealed evenly distributed dimples on the fracture surface indicating the ductile mode of failure.

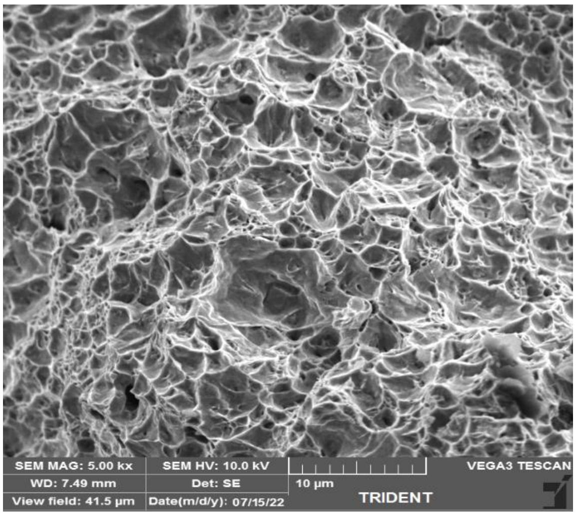

Fig. 14. Fracture morphology of failed LH74 weldment after tension test.

3.5. Corrosion Behaviour

Polarization test is conducted for evaluating the corrosion performance of base metal and welded samples. For evaluating the corrosion resistance of the samples, test is performed in 3.5% NaCl solution with constant specimen's surfaces area 0.1257 cm^2 at room temperature. The polarization measurements are noted by the potential with a range of -250 mV to +550 mV with respect to SCE corrosion potential (Ecorr) at scan rate of 10 mV/s. Polarization characteristic curves for LH74, LH86 and BM samples are shown in Fig. 15.

The linear segments of the anodic and cathodic curves are extrapolated for corrosion potentials to evaluate the corrosion current densities (Icorr). Icorr calculated in the range of Ecorr= ±25 mV according to Stern-Geary equation 2 [35].

$$I_{corr} = \left(\frac{\beta_a \times \beta_b}{2.303.R_p(\beta_a+\beta_b)}\right) \tag{2}$$

The corrosion rate (CR), is calculated as

$$CR=3.27\times 10^{-3}\ Icorr \times (Ew/\rho) \tag{3}$$

Where E_w is equivalent weight in gms and ρ is the density in g/cm^3.

Fig. 15 shows the curves of potentiodynamic polarization for base LDSS2101 sample and LH74 and LH86 welded samples. Tafel extrapolation is used to find the passivation current density in mA/cm^2 (Ipass), pitting potential in mV (Epit), corrosion current density in mA/cm^2 (Icorr), corrosion potential in mV (Ecorr) and corrosion rate in mm/yr.

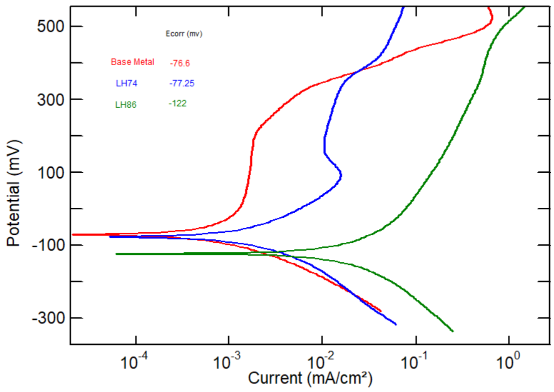

Fig. 15. Potentiodynamic polarization curve for base LDSS2101 sample and LH74 and LH86 welded samples.

These characteristics values obtained from test are summarized in Table 5. From the table, It can be seen that LH74 sample shows the lowest corrosion current (Icorr= 0.0045 mA/cm^2) and LH86 sample depicts high corrosion current 0.1251 mA/cm^2 with limited or no passivation. The LH86 sample shows high corrosion rate in comparison with LH 74 and BM, i.e. lowest corrosion resistance. LH 74 sample shows least corrosion rate i.e. highest corrosion resistance. This is due to high percentage of chromium concentrations that can be noticed in Table 3 [25]. Epit is the potential when stable pits forms. The Epit values are directly proportional to the pitting corrosion resistance of the material [36]. LH74 sample has best Epit which showing high resistant to the localized corrosion. LH74 sample exhibited strong passive behaviour because of the oxidant solution whereas in the LH86 and BM samples, the passivation zone is less pronounced. From Fig. 15, it is clear that the LH86 weld has the least pitting potential hence low resistance to pitting corrosion, this is because of the increasing of coarse austenite grains. From the results, the lowest corrosion current density and the noblest corrosion potential are measured for LH74 sample.

4. CONCLUSIONS

The influence of heat inputs on weldments was investigated on the lean duplex stainless steel. The LDSS2101 carried out GTA welding with ER2209 electrode for two different heat input conditions. Material characterization for the welded 2101 samples was examined by optical microscopy, scanning electron microscopy equipped with EDS and XRD analysis. Hardness of the LDSS2101 was evaluated for base and welded samples. Potentiodynamic polarization test was conducted to understand the corrosion resistance in the weldments. Microstructural behaviour for variable heat conditions on GTAW was the focus of this work. From the experimental results, the following conclusions were drawn:

- Good, formed welds with no carbide's precipitation in weld metal and heat affected zone in both heat inputs were carried out for GTAW.
- The microstructure consisted of austenite and ferrite phases and with the heat input increase there was a decrease in ferrite content. The heat inputs had significant effect on the microstructure.
- The amount of austenite precipitation increased with the increase in the heat input during welding, thereby leading to slpw cooling rate

Table 5. Corrosion parameters obtained from Potentiodynamic polarization curves

sample	Ecorr (mv)	Icorr (mA/cm^2)	Epit (mv)	Ipass (mA/cm^2)	Corrosion rate (mm/yr)
Base	-76.6	0.0535	234	1.2521	**0.5729**
LH74	-77.25	0.0045	342	0.0176	**0.0487**
LH86	-122	0.1251	326	0.516	1.3389

[DOI: 10.22068/ijmse.2792]

after welding. In addition to heat input, filler metal ER2209 with enriched Ni content played a major role in the stabilization of the austenite phases in the weldment.

- At high heat input 1.3 kJ/mm, hardness value was decreased. The weld metal had high hardness for low heat input condition. Increasing the heat input decreased the hardness and this could be attributed to phase ratio and cooling rate.
- Potentiodynamic cyclic polarization tests revealed that the low heat input welded sample possessed the highest pitting potential, indicating the highest resistance to pitting.
- The curves of polarization show that the low heat input welded sample showed increased corrosion resistance as compared to the high heat weldment. These are due to the low passive current density obtained for 0.85 kJ/mm heat input.

REFERENCES

[1] Bassani, P., Breda, M., Brunelli, K., Mészáros, I., Passaretti F., Zanellato, M., and Calliari, I., "Characterization of a cold-rolled 2101 lean duplex stainless steel." Microsc. Microanal., 2013, 19, 988–995.

[2] Zhang, L., Jiang, Y., Deng, B., Zhang, W., Xu, J., and Li, J., "Effect of aging on the corrosion resistance of 2101 lean duplex stainless steel." Mater. Charact., 2009, 60, 1522–1528.

[3] Lippold, J. C., and Kotecki, D. J., Welding Metallurgy and Weldability of Stainless Steels, Wiley-Interscience, 2005.

[4] Liljas, M., Johansson, P,. Liu, H. P., and Olsson C. O. A., "Development of a Lean Duplex Stainless Steel." steel research int., 2008, 79, 466– 473.

[5] Gunn, R., Duplex Stainless Steels: Microstructure, Properties and Applications, 1st edn. Woodhead Publishing, 1997.

[6] Deng, B., Jiang, Y., Xu, J., Sun, T., Gao, J., Zhang, L., Zhang, W., and Li, J., "Application of the modified electrochemical potentiodynamic reactivation method to detect susceptibility to intergranular corrosion of a newly developed lean duplex stainless steel LDX2101." Corros. Sci., 2010, 52, 969–977.

[7] Sieurin, H., Sandström, R., and Westin, E. M., "Fracture toughness of the lean duplex stainless steel LDX 2101." Metall. Mater. Trans. A Phys. Metall. Mater. Sci., 2006, 37, 2975–2981.

[8] Olsson, J., and Snis, M., "Duplex - A new generation of stainless steels for desalination plants." Desalination, 2007, 205, 104–113.

[9] "Achieving material cost predictability in the pulp and paper industry with lean duplex stainless steel", Outokumpu Stainless AB, https://www.outokumpu.com/en/expertise.

[10] Mehta, K., Advanced Joining and Welding Techniques: An Overview. Advanced Manufacturing Technologies, ed. K. Gupta. Springer, Cham, 2017, 101-136.

[11] Pilhagen, J., and Sandström, R., "Influence of nickel on the toughness of lean duplex stainless steel welds." Mater. Sci. Eng. A, 2014, 602, 49–57.

[12] Verma, J., and Taiwade, R. V., "Effect of welding processes and conditions on the microstructure, mechanical properties and corrosion resistance of duplex stainless steel weldments—A review." J. Manuf. Process., 2017, 25, 134–152.

[13] Muthupandi, V., Bala Srinivasan, P., Seshadri, S. K., and Sundaresan, S., "Effect of weld metal chemistry and heat input on the structure and properties of duplex stainless steel welds." Mater. Sci. Eng. A, 2003, 358, 9–16.

[14] Sadeghian, M., Shamanian, M., and Shafyei, A., "Effect of heat input on microstructure and mechanical properties of dissimilar joints between super duplex stainless steel and high strength low alloy steel." Mater. Des., 2014, 60, 678–684.

[15] Mortazavi, E., Najafabadi, R. A., and Meysami, A., "Effect of heat input on microstructure and mechanical properties of dissimilar joints of AISI 316l steel and API X70 high-strength low-alloy steel." J. Iron Steel Res. Int., 2017, 24, 1248–1253.

[16] Taban, E., and Kaluc, E., "Welding behaviour of duplex and superduplex stainless steels using laser and plasma arc welding processes." Weld World, 2011, 55, 48–57.

[DOI: 10.22068/ijmse.2792]

[17] Capello, E., Chiarello, P., Previtali, B., and Vedani, M., "Laser welding and surface treatment of a 22CrÁ/ 5NiÁ/ 3Mo duplex stainless steel." Mater. Sci. Eng. A, 2003, A351, 334–343.
[18] Amigó, V., Bonache, V., Teruel, L., and Vicente, A., "Mechanical properties of duplex stainless steel laser joints." Weld. Int., 2006; 20, 361–366.
[19] Westin, E. M., and Hertzman, S., "Element distribution in lean duplex stainless steel welds." Weld World, 2014, 58, 143–160.
[20] Ha, H. Y., Lee, T. H, Lee, C. G., and Yoon. H., "Understanding the relation between pitting corrosion resistance and phase fraction of S32101 duplex stainless steel." Corros. Sci., 2019, 149, 226–235.
[21] Westin, E. M., and Fellman, A., "Effect of laser and laser hybrid welding on the corrosion performance of a lean duplex stainless steel." J. Laser Appl., 2010, 22, 150–158.
[22] Brytan, Z., and Niagaj, J., "Corrosion resistance and mechanical properties of TIG and A-TIG welded joints of lean duplex stainless steel S82441/1.4662." Arch. Metall. Mater., 2016, 61, 771–784.
[23] Reka Fabian E., "Laser Welding Parameters Effect on the Weld Metals Properties at Duplex Stainless Steels." Adv. Technol. Mater., 2018, 43, 7–13.
[24] Parmar R. S., Welding Engineering & Technology, Khanna Publisher. New Delhi, 2002.
[25] Ouali, N., Khenfer, K., Belkessa, B., Fajoui, J., Cheniti, B., Idir, B., Branchu, S., "Effect of Heat Input on Microstructure, Residual Stress, and Corrosion Resistance of UNS 32101 Lean Duplex Stainless Steel Weld Joints." J. Mater. Eng. Perform., 2019, 28, 4252–4264.
[26] "Standard practice for preparation of metallographic specimens", E3–95. ASTM. PA, USA, 1995.
[27] "Metallographic and Microstructures", ASM International, Materials Park, Ohio, USA, 2004.
[28] Bao, L., Wang, Y., and Han, T., "Microstructure and properties of lean duplex stainless steel uns s32101 welded joint by hot wire tig welding." Materials Science Forum., 2020, 993, 466–473.
[29] Kumar, N., Kumar, A., Gupta, A., Gaikwad, A. D., and Khatirkar, R. K., "Gas Tungsten Arc Welding of 316L Austenitic Stainless Steel with UNS S32205 Duplex Stainless Steel." Trans. Indian Inst. Met., 2018, 71, 361–372.
[30] Nowacki, J., and Łukojc. A., "Microstructural transformations of heat affected zones in duplex steel welded joints." Mater. Charact., 2006, 56, 436–441.
[31] Shin, Y. T., Shin, H. S., and Lee, H. M., "Effects of Heat Input on Pitting Corrosion in Super Duplex Stainless Steel Weld Metals." Met. Mater. Int., 2012, 18, 1037–1040.
[32] Yang Y., Yan, B., Li, J., and Wang, J., "The effect of large heat input on the microstructure and corrosion behaviour of simulated heat affected zone in 2205 duplex stainless steel." Corros. Sci., 2011, 53, 3756–3763.
[33] Mortazavi, E., Najafabadi, R, A., and Meysami, A., "Effect of Heat Input on Microstructure and Mechanical Properties of Dissimilar Joints of AISI, 316L Steel and API X70 High-Strength Low-Alloy Steel." J. Iron. Steel Res. Int., 2017, 24, 1248–1253.
[34] Paulraj, P., and Garg, R., "Effect of welding parameters on mechanical properties of GTAW of UNS S31803 and UNS S32750 weldments." Manufacturing Rev. 2015, 29(2), 1-9.
[35] Brytan, Z., Niagaj, J., and Reiman., "Corrosion studies using potentiodynamic and EIS electrochemical techniques of welded lean duplex stainless steel UNS S82441." Appl. Surf. Sci., 2016, 388, 160–168.
[36] Ma, C. Y., Zhou, L., Zhang, R. X., Li, D. G., Shu, F. Y., Song, X. G., and Zhao, Y. Q., "Enhancement in mechanical properties and corrosion resistance of 2507 duplex stainless steel via friction stir processing." J. Mater. Res. Technol. 2020, 9, 8296–8305.